npj | 2D Materials and Applications

www.nature.com/npj2dmaterials

ARTICLE OPEN

Check for updates

Two dimensional V_2O_3 and its experimental feasibility as robust room-temperature magnetic Chern insulator

Simon Mellaerts[1]✉, Ruishen Meng[1], Mariela Menghini[1,2], Valeri Afanasiev[1], Jin Won Seo[3], Michel Houssa[1,4] and Jean-Pierre Locquet[1]

The possibility of dissipationless chiral edge states without the need of an external magnetic field in the quantum anomalous Hall effect (QAHE) offers a great potential in electronic/spintronic applications. The biggest hurdle for the realization of a room-temperature magnetic Chern insulator is to find a structurally stable material with a sufficiently large energy gap and Curie temperature that can be easily implemented in electronic devices. This work based on first-principle methods shows that a single atomic layer of V_2O_3 with honeycomb–kagome (HK) lattice is structurally stable with a spin-polarized Dirac cone which gives rise to a room-temperature QAHE by the existence of an atomic on-site spin–orbit coupling (SOC). Moreover, by a strain and substrate study, it was found that the quantum anomalous Hall system is robust against small deformations and can be supported by a graphene substrate.

npj 2D Materials and Applications (2021)5:65 ; https://doi.org/10.1038/s41699-021-00245-w

INTRODUCTION

To advance electronics at the nanoscale, the exploration and exploitation of quantum degrees of freedom in materials become indispensable. Two-dimensional (2D) compounds form excellent systems, wherein these quantum degrees of freedom can be exploited toward electronic and spintronic applications. A particular group of interest is 2D *Dirac materials*, which have a Dirac cone with linear dispersion in their band structure[1]. These materials have been predicted to exhibit a large variety of exotic properties: massless fermions[2], ultrahigh carrier mobility[3], (fractional) quantum Hall effects (QHE)[4,5], etc. Furthermore, there have been great advances in the preparation and growth of 2D materials in recent years[6–8], which initiated the study of the largely unexplored group of 2D strongly correlated Dirac systems (SCDS). As the Dirac cone has shown to be instrumental for the realization of many nontrivial topological phases[9,10], these SCDS uncover a rich playground where relativistic dispersion, electron correlations, and topological ordering meet.

In this work, we perform an ab initio study on the 2D single atomic layer of V_2O_3 with honeycomb–kagome (HK) lattice structure. First, we confirm the predicted[11] ground-state properties of HK V_2O_3 and establish that it is an excellent SCDS candidate with a room-temperature QAHE. The second part of this work mainly focuses on the experimental feasibility by studying the structure under compressive and tensile biaxial strain as well as the graphene-supported V_2O_3 monolayer system.

RESULTS

Structural stability and mechanical properties

The structurally optimized unit cell of HK V_2O_3 is shown in Fig. 1a with a planar HK lattice with a lattice constant 6.193 Å. A reduction of 0.15 Å of the V–O bond—from 1.94 to 1.79 Å—is found compared to the shortest V–O bond in bulk V_2O_3[12]. A similar reduction is observed in other metal oxides[13–15]. This can be attributed to the reduction in coordination number of the V^{3+} cation in this 2D form, where V^{3+} has the electron configuration [Ar]$3d^2$ with the two outer 4*s* electrons of vanadium ionically bonded to the oxygen. The structural stability is firstly examined by calculating the formation energy $E_{form} = E_{V_2O_3} - 2E_V - 3/2\mu_{O_2}$ with $E_{V_2O_3}$ and E_V are the total energies of the HK V_2O_3 and V crystal structure (−8.934 eV/atom), while $\mu_{O_2} = -4.9480$ eV/atom is the chemical potential oxygen gas. The obtained negative value of −1.81 eV/atom (compared to −2.29 eV/atom in bulk V_2O_3) together with earlier experimental work[16] suggests the experimental feasibility of the system.

To study the dynamical stability of the monolayer system, the phonon spectrum was evaluated by DFPT. As shown in Fig. 1b, the spectrum shows no imaginary frequency phonon modes, confirming the dynamical stability. Furthermore, the AIMD simulation at a fixed temperature of 300 K also confirmed the thermal stability, since total energy fluctuations of only 0.3% are observed while planarity is preserved, as shown in Fig. 1c, d. In addition, the elastic properties and stability were verified (see Supplementary Table 1). Therefore, it can be concluded that the single atomic layer of V_2O_3 with HK lattice structure is stable on all three levels: dynamical, thermal, and mechanical.

Magnetic ground state

To determine the magnetic ground state of the system, various magnetic configurations have been studied. By the use of noncollinear calculations with SOC, the total energy of the ion–electron system was determined for ferromagnetic (FM), nonmagnetic (NM), and four types of antiferromagnetic (AFM) states, depicted in Fig. 2a. By comparison of the total energies in Table 1, it can be concluded that the system is in a FM ground state, with the AFM stripy (AFM-ST) state as the second-lowest energy state. As a first approximation, we assume an isotropic exchange interaction (i.e., neglecting anisotropic exchange), and consider the following spin hamiltonian,

$$H = -\sum_{\langle i,j \rangle} J_1 \mathbf{S}_i \cdot \mathbf{S}_j - \sum_i A(\mathbf{S}_i^z)^2 \quad (1)$$

[1]Department of Physics and Astronomy, KU Leuven, Leuven, Belgium. [2]IMDEA Nanociencia, Madrid, Spain. [3]Department of Materials Engineering, KU Leuven, Leuven, Belgium. [4]Imec, Kapeldreef 75, Leuven, Belgium. ✉email: simon.mellaerts@kuleuven.be

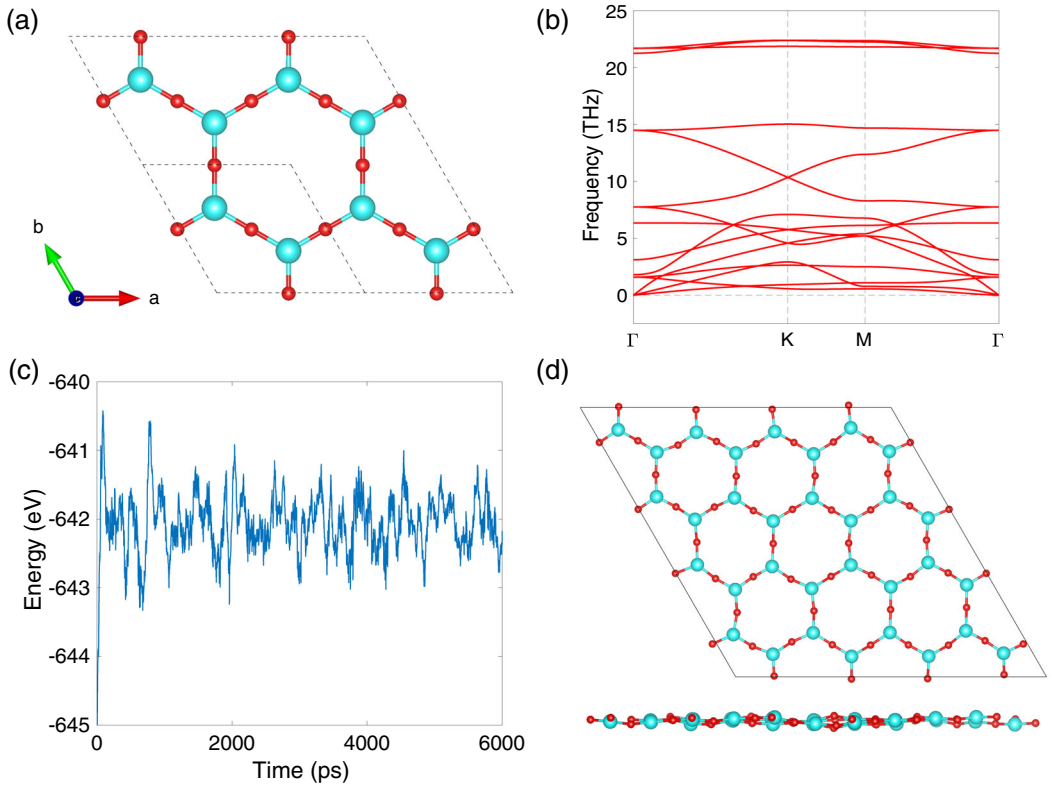

Fig. 1 V_2O_3 monolayer and its structural stability. a The (2 × 2) supercell of the HK V_2O_3 monolayer with the unit cell indicated by dashed lines and cyan and red representing the V and O atoms, respectively. **b** The calculated phonon band dispersion. **c** The energy fluctuations during AIMD and **d** the atomic structure obtained after 6000 ps.

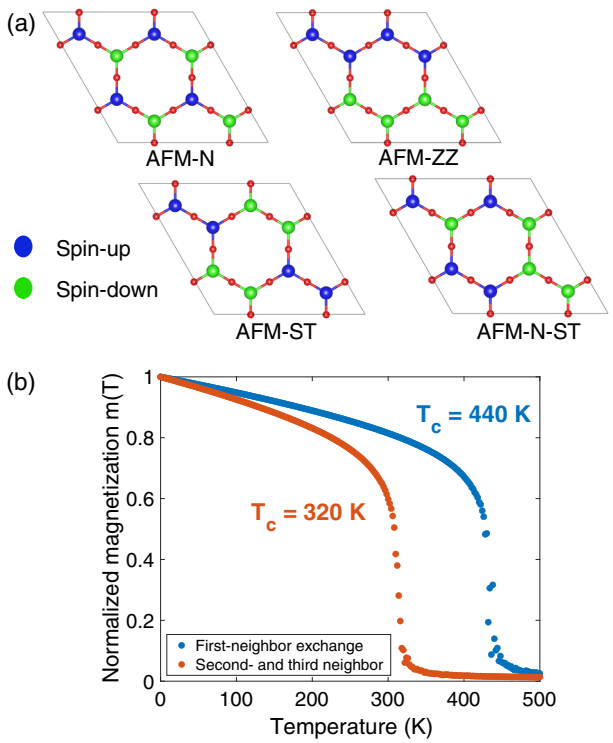

Fig. 2 Magnetic configurations and Curie temperature. a Top view of various possible AFM configurations. **b** The normalized magnetization as a function of the temperature from the MC simulations indicating a $T_c = 440$ K.

Table 1. The DFT calculated energies (eV/f.u.) for different (out-of-plane) magnetic configurations with respect to the lowest FM energy state which is set to zero.

Magnetic ordering	FM	NM	AFM-N	AFM-ST	AFM-ZZ	AFM-N-ST
Energy (eV/f.u.)	0	1.54	0.35	0.18	0.20	0.42

where i enumerates the magnetic ions. The first term is the nearest-neighbor exchange interaction with exchange parameter J_1, while the second term corresponds to the single-ion anisotropy with the anisotropy parameter A. The interaction is ferromagnetic when $J_1 > 0$ and positive A will favor an out-of-plane spin component $\mathbf{S}^z$.

The exchange parameter is evaluated by $J_1 = [E_{AFM} - E_{FM}]/2zS^2$ with the total spin moment $S = 1$, and with $z = 3$ neighboring spins. This gives $J_1 = 58$ meV. On the other hand, the magneto-crystalline anisotropy energy (MAE) defined by $E_{MAE} = E_{[100]} - E_{[001]}$, with square brackets indicating the orientation of the spins, equals 2 meV/f.u. (i.e., $A = 1$ meV). This strong MAE can be understood from degenerate perturbation theory. The SOC-induced interaction involves the coupling between states with identical spin, with the most important interaction between the unoccupied and occupied d states. As can be seen in Fig. 3b, these states at the conduction band minimum (CBM) at Γ and valence band maximum (VBM) at K, respectively, consist of the $(d_{xy}, d_{x^2-y^2})$- and (d_{xz}, d_{yz}) orbitals. This SOC-induced interaction involves a change in the orbital angular momentum quantum number L_z from (d_{xz}, d_{yz}) with $L_z = \pm 1$ to $(d_{xy}, d_{x^2-y^2})$ with $L_z = \pm 2$. This interaction between these out-of-plane spins leads to a

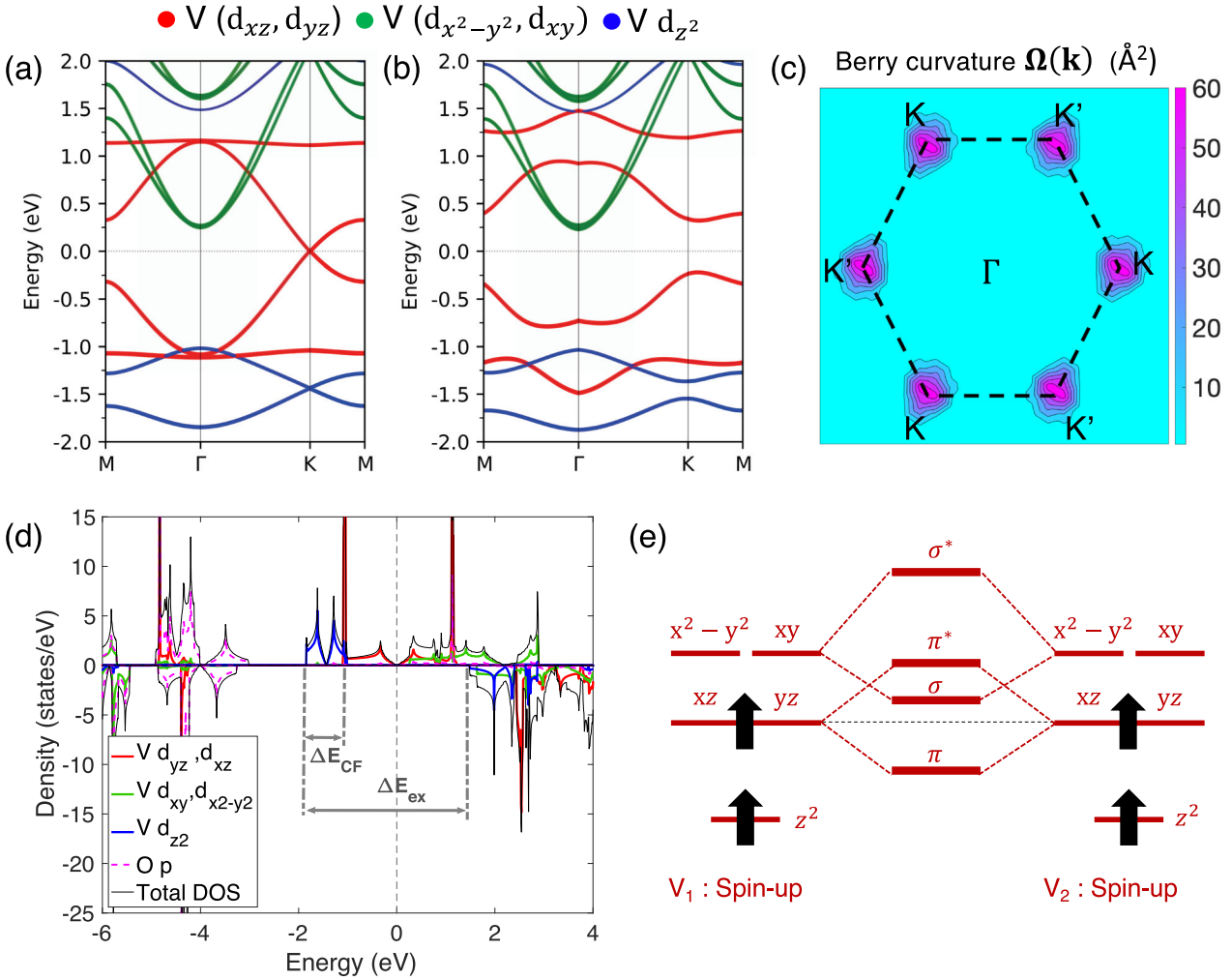

Fig. 3 Electronic band structure with derived orbital and topological character. a The electronic band structure within GGA+*U* without SOC and (**b**) with SOC. **c** The calculated Berry curvature projected onto the BZ. **d** The orbital- and spin-resolved DOS. **e** The derived orbital ordering and bonding of the spin-polarized V 3*d* orbitals.

maximization of the SOC energy stabilization, as described in ref. [17].

To obtain an estimate of the Curie temperature (T_c), the Curie–Bloch equation in the classical limit,

$$m(T) = \left(1 - \frac{T}{T_c}\right)^{\beta} \tag{2}$$

with T the temperature and β a critical exponent, is fitted to the normalized magnetization obtained by the MC simulation (see Fig. 2b). The resulting T_c is equal to 440 K with $\beta = 0.19$, and can also be compared within the mean-field approximation for the honeycomb lattice (ignoring the ion anisotropy) by using the formula[18],

$$T_c = \frac{3J_1}{2k_B} S^2 \tag{3}$$

with Boltzmann constant k_B, resulting in $T_c = 1010$ K, which gives the usual overestimation of the critical temperature.

Since the Néel AFM phase is not the second-lowest energy state, it can be expected that second- and third-neighbor exchange interactions (J_2, J_3) are playing a dominant role in the magnetic ordering. Therefore, the DFT total energies were mapped onto the Ising hamiltonian to obtain J_1, J_2, and J_3 by the following four equations:

$$E_{FM/AFM-N} = E_{NM} - (\pm 3J_1 + 6J_2 \pm 3J_3)S^2, \tag{4}$$

and

$$E_{AFM-ZZ/ST} = E_{NM} - (\pm J_1 - 2J_2 \mp 3J_3)S^2. \tag{5}$$

The J_1, J_2, and J_3 values were found to be 41.9, −3.8, and 17.4 meV, respectively. Taking into account, these second- and third-neighbor exchange interactions in the spin hamiltonian (1), the hamiltonian is solved by the MC simulation, with the magnetization (shown in Fig. 2) fitted by Eq. (2), giving a Curie temperature equal to 320 K with $\beta = 0.20$.

Electronic structure

The electronic band structure and density of states (DOS) within GGA+*U* are depicted in Fig. 3. The electronic band structure shows two key features: a Dirac cone at the *K* point and the existence of two flat bands at ± 1 eV forming a degeneracy with the dispersive bands at the Γ point. From the DOS, it becomes clear that there exists a strong spin polarization with the two characteristic band features being derived from the spin-up V (d_{xz}, d_{yz}) orbitals. This means that the Dirac cone is completely spin-polarized, making it a Dirac spin-gapless semiconductor (DSGS)[19].

Table 2. The calculated direct and indirect energy gap E_g values for the different exchange-correlation functionals with SOC included.

	LDA+U	GGA+U	HSE06
Direct E_g (eV)	0.37	0.54	1.54
Indirect E_g (eV)	0.19	0.45	1.52

By taking into account the intrinsic SOC, it is found that an energy gap is opened at the K point, resulting in an indirect energy gap of 0.45 eV. It turns out that the energy gap is strongly dependent on the Hubbard correction U (see Supplementary Fig. 3), which has led to the idea of the cooperative effect between electron correlations and SOC. The relatively large energy gap opened at the Dirac point can be understood from the fact that the orbital degeneracy of the occupied states allows an *atomic* on-site SOC, involving no hopping process[20]. This is in contrast to the second-order hopping SOC in the Kane–Mele model, or the first-order hopping SOC in the Xenes[21]. Within this understanding, it is clear that an increase of U will force the electrons into a more localized state implying an increased effect of the atomic SOC[22,23].

In addition to the GGA+U, the LDA and hybrid exchange-correlation functional HSE06 were used to study the electronic properties of the system. The resulting energy gap values are summarized in Table 2, and the calculated band structures can be found in Supplementary Fig. 4. It is noted that there is a strong variation of the energy gap depending on the chosen functional. This can be expected as these functionals are approximating the localized nature of the 3d orbitals very differently, which will be crucial for the atomic SOC effect.

This exchange-correlation functional dependence is informative and sheds light on the physical nature of the interplay of electron correlations and SOC in opening the gap at the Dirac cone. However, it should be kept in mind that the GGA+U (with $U =$ 3 eV) is considered as the most accurate description as the electron correlations (U) have been estimated on the basis of a first-principle linear response method, while it is well-known that the HSE06 overestimates the bandgap of bulk V_2O_3 and other TMO[24,25].

From the DOS, it can be inferred that the crystal field splits the d-orbitals into three orbital levels whose energy ordering can be derived from the orbital orientation. The d_{z^2}-orbital level has negligible overlap with the O 2p orbitals and thus has the lowest energy state, the (d_{xz}, d_{yz})-orbitals oriented out-of-plane will form a π-bond with the oxygen O p_z as bridging ligand, and the $(d_{xy}, d_{x^2-y^2})$-orbitals will form an in-plane σ-bond with bridging orbitals O (p_x, p_y). This latter bond involves a strong orbital overlap and therefore the involved orbitals will be energetically less favorable, forming the highest energy state. The resulting orbital ordering is shown in Fig. 3e. It should be emphasized that in the vicinity of the Fermi level, there is approximately no O 2p orbital weight, which confirms the localized nature of the two V 3d electrons. Based on Griffith's crystal-field theory[26], the spin state of the V^{3+} cation can be confirmed. By the relative strengths of the exchange (ΔE_{ex}) and crystal-field splitting (ΔE_{CF}) with derived values of 3.34 eV and 0.8 eV—it can be concluded that the V cation has a high ($S = 1$) spin state with magnetic moment 2 μ_B.

To gain further insight into the nature of the chemical bond, the atomic charges were determined by the Bader charge analysis code[27]. It is found that the atomic charges on V and O are resp. $Q_V = 1.59e$ and $Q_O = -1.07e$, confirming the ionic bonding character where the electrons of the V cation are attracted toward the O anion. Nevertheless, the atomic charges are slightly lower than in the bulk parent, which suggests that there is an increased electron delocalization and thus stronger bonding covalency compared to the bulk. This behavior can be linked to the reduced V–O bond length. On the other hand, the relative strong ionicity of the bond might explain the energetic stability of the planar configuration of these TMO monolayer systems, since the buckling of the V–O bond would result in an energetically unfavorable large dipole moment normal to the atomic plane. In this way, the reduced bond length and enhanced covalency can be explained as a means to suppress the possible large dipole moment. These trends and their explanations were already pointed out for other TMOs[13,14].

To study the topology of the band structure, the Berry curvature $\mathbf{\Omega}(\mathbf{k})$ of the system was calculated directly from the DFT calculated wave functions by the VASPBERRY code, which is based on Fukui's method[28]. The resulting Berry curvature, shown in Fig. 3c, becomes nonzero at the Dirac points K and K′. By integrating the Berry curvature $\mathbf{\Omega}_n(\mathbf{k})$ of each nth energy band over the whole BZ and summing over all occupied bands, the Chern number

$$C = \sum_n \frac{1}{2\pi} \int_{BZ} d^2\mathbf{k}\ \Omega_n(\mathbf{k}) \tag{6}$$

is found to be $C = 1$. Therefore, it can be concluded that the system is a room-temperature Chern insulator.

Moreover, the Berry curvature and resulting Chern number $C =$ 1 were found to be robust against the Hubbard value U. However, by evaluating the Berry curvature of the HSE06 band structure, a Chern number equal to zero was found (see Supplementary Fig. 6). Although the experimental validity of the HSE06 band structure can be critically questioned, it shows the intimate interplay of electron correlations and topology. The electron correlations causing a topological phase transition to a trivial state agree well with earlier theoretical studies[22,29], and it opens great opportunities as the magnitude of electron correlations can be more easily controlled externally in Dirac materials[30,31].

Biaxial strain

TMOs are known to exhibit a rich-phase diagram as a function of strain, in particular, for bulk V_2O_3 the room-temperature metal–insulator transition (MIT) between the paramagnetic insulating and metallic state can be realized by the application of epitaxial strain[32]. Therefore, a biaxial strain study on the 2D atomic layer of V_2O_3 was performed. The atomic positions were optimized for all biaxially strained configurations from − 10% to + 10%. It was found that under compressive strain, the lattice structure undergoes an in-plane buckling of the V–O bond (HK_{in}), as can be seen in Fig. 4a, b. This structural distortion is found by ionic relaxation with a high force-convergence criterion of 0.005 eV/Å. On the other hand, by lowering the force-convergence criterion to 0.05 eV/Å, two metastable structures were found in the compressive region; one preserving the HK lattice structure (HK), while the other undergoes an out-of-plane buckling of the V–O bond (HK_{out}). Although these lattice configurations are un/metastable, they could become stabilized under certain conditions and depending on underlying substrates. Moreover, a combination of in- and out-of-plane buckling can also be expected and was observed in an ab initio calculation of TMOs on metal substrates[33].

Identifying these different structural configurations under compressive strain in the freestanding V_2O_3 monolayer allows a further study on the structural stability and provides a better understanding of the involved chemical bonds governing the stability of this planar single atomic layer. From the structural in- and out-of-plane distortions, it is noted that the deformation of the V–O bond develops to prevent a further reduction of this bond length (see Fig. 4c). This behavior can be linked to the ionic character of the bond. On the other hand, from the energetic point of view, the system prefers to undergo an in-plane deformation rather than the out-of-plane deformation. This can be attributed to the energy cost of the formation of a dipole moment under a buckling of the V–O bond.

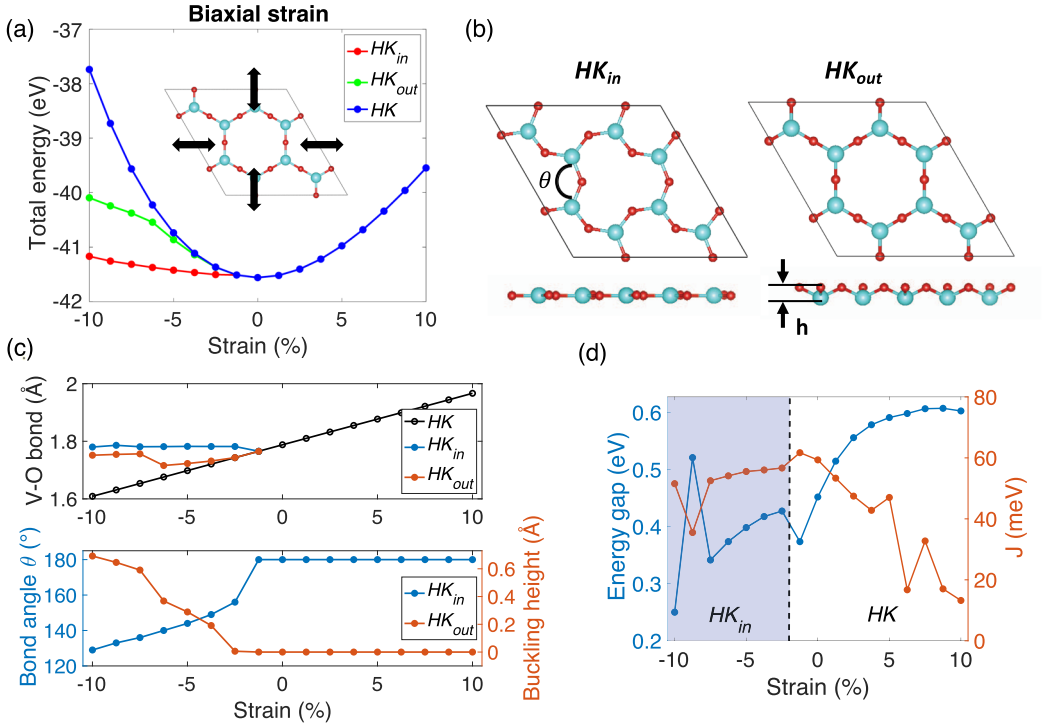

Fig. 4 Biaxial strain study. a The total energy of the system under biaxial strain, taking into account (**b**) the possible structural deformations (HK_{in}, HK_{out}) with deformation parameters the bond angle θ and the buckling height h, respectively. **c** Top: the V–O bond length as a function of strain for all three configurations. Bottom: the bond angle θ and buckling height h in function of the strain for resp. HK_{in} and HK_{out}. **d** The energy gap and magnetic exchange interaction as a function of strain.

In addition to this structural study, the electronic and magnetic properties as a function of the biaxial strain were studied. Since the stabilization of the metastable states (*HK* and HK_{out}) will depend on external conditions, only the most stable HK_{in} configuration is considered for the compressive region. The energy gap and the magnetic exchange interaction are shown in Fig. 4. It is clear that within the strain range of −5 to +5%, the electronic and magnetic properties are sufficiently preserved to maintain the room-temperature magnetic Chern insulating phase. It was also confirmed that the Chern invariant *C* remains equal to 1, even in the presence of the in-plane distortion of HK_{in}. This can be expected as the V cations still form a honeycomb lattice, crucial for the existence of the Dirac cone[34]. From these results, it can be concluded that the room-temperature QAHE in 2D V_2O_3 is robust against small structural deformations.

Graphene substrate

Motivated by the successful deposition of Y_2O_3 on graphene[35], the feasibility of using a graphene substrate for the growth of the V_2O_3 monolayer was studied. A (2 × 2) V_2O_3 supercell on a (5 × 5) graphene supercell was structurally optimized and that configuration is shown in Fig. 5a (see Supplementary Note 2). Similar to Al_2O_3 and Y_2O_3 monolayers on graphene[13,14], the V cations are located near the top sites of the C atoms to maximize the potential bonding. The planar HK lattice structure is conserved with a minimal distance between graphene and V_2O_3 of 3.43 Å, while the V–O bond length remains approximately preserved.

To obtain a first estimate of the interfacial interaction strength, the adsorption energy E_{ad} is determined,

$$E_{ad} = E_G + E_{V_2O_3} - E_{G+V_2O_3} \quad (7)$$

where E_G, $E_{V_2O_3}$, and $E_{G+V_2O_3}$ are the total energies of the isolated graphene, isolated V_2O_3, and the combined hybrid structure, respectively. The adsorption energy equals 77 meV per C atom indicating a weak interaction between both monolayers, albeit stronger than for HK Y_2O_3 on graphene (42 meV per C atom)[14].

To preserve the electronic properties, it is important to prevent charge transfer between both monolayers, therefore the atomic charges of the systems were determined for the hybrid system. The average atomic charges of both V and O remain unchanged, while the average excess charge of the C atom is only 0.004*e*. This indicates negligible electron transfer between both monolayers, which can also be confirmed by the calculation of the charge density difference $\Delta\rho = \rho_{G+V_2O_3} - \rho_G - \rho_{V_2O_3}$, shown in Fig. 5b. The charge density difference shows a negligibly small inhomogeneous charge distribution between both monolayers, which is mainly located between V and C atoms. This indicates a small orbital hybridization of the π-bonded orbitals of V_2O_3 and graphene. This is similar to earlier studies of HK TMOs on graphene where it was shown that vdW interactions and orbital hybridization play an important role in the electronic properties at the interface[13,14].

The electronic properties of the V_2O_3 monolayer on the graphene substrate are shown in Fig. 5c, d. From the band structure and DOS, it is noted that the conduction band minimum of graphene is about 0.2 eV below the Fermi level, indicating that graphene is slightly n-doped. A similar n-doping of graphene was found for HK Y_2O_3[14]. The DOS contribution of the V_2O_3 remains approximately preserved, however from the calculated band structure, it is clear that there is some hybridization of the π-bonded orbitals. Nonetheless, the Dirac cone of V_2O_3 remains preserved with a reduction in the SOC-induced direct energy gap to 66 meV.

Overall the HK V_2O_3 monolayer on graphene shows very similar behavior to HK Y_2O_3[14] in terms of vdW bonding—as can be seen from the Bader charge analysis, charge density difference, and the

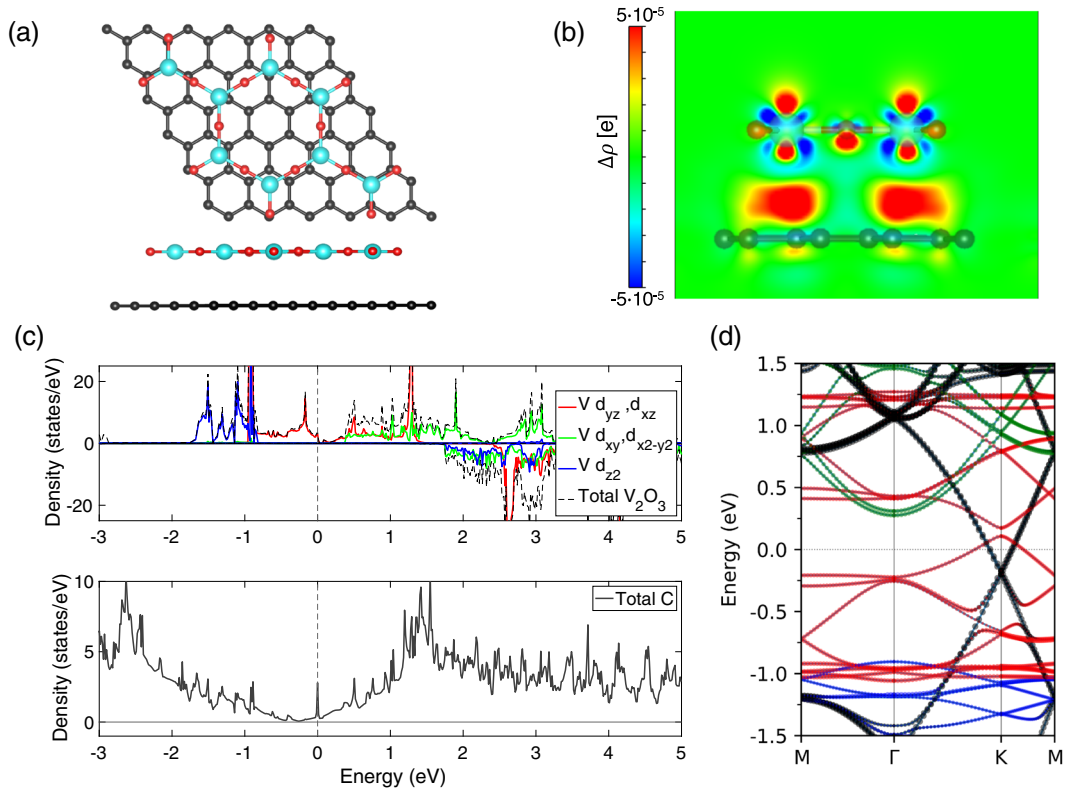

Fig. 5 Graphene substrate study. a The top and side view of (2 × 2) V_2O_3 supercell on a (5 × 5) graphene supercell. **b** The calculated charge density difference $\Delta\rho$ where blue and red correspond to excess and depleted charge density, respectively. **c** The DOS within GGA+*U* and (**d**) band structure of 2D HK V_2O_3 op graphene within GGA+*U*+SOC. The color code is the same used in (**c**).

effect on the electronic structure. Therefore, based on the successful deposition of Y_2O_3 on graphene[35] together with the results in the section "structural stability and mechanical properties" and early experimental work[16], it is expected that graphene might be an optimal substrate for the growth of the V_2O_3 monolayer.

DISCUSSION

In this work, we have confirmed that the single atomic layer of V_2O_3 with HK lattice structure is a structurally stable room-temperature magnetic Chern insulator. This system features the coexistence of topological order and strong electron correlations, and might therefore be an excellent SCDS candidate. It was shown that the system can undergo small structural deformations which preserve the honeycomb lattice of the V cations, such that the Dirac cone and the corresponding room-temperature QAHE remain unaffected. Furthermore, this 2D V_2O_3 can be further stabilized by the support of a graphene substrate, where there is only a small interfacial interaction mainly attributed to orbital hybridization, but preserving the Dirac cone of both materials. These observations together with earlier studies on TMO with HK lattice structure[13–15,35–39] should encourage the experimental investigation of this group of 2D TMOs.

METHODS

DFT calculations

All spin-polarized calculations were carried out within density-functional theory (DFT), as implemented in the Vienna ab initio simulation package (VASP)[40]. The generalized gradient approximation (GGA) in the form of Perdew–Burke–Ernzerhof (PBE)[41], projected-augmented-wave (PAW) potential[42], and the plane-wave basis with an energy cutoff of 550 eV were used. For the structural relaxation, a force-convergence criterion of 0.005 eV/Å was used with the Brillouin zone (BZ) sampled by a 12 × 12 × 1Γ-centered *k*-point mesh, with a vacuum space of 17 Å adopted along the normal of the atomic plane. To account for the localized nature of the 3*d* electrons of the V cation, a Hubbard correction *U* is employed within the rotationally invariant approach proposed by Dudarev et al.[43], where $U_{\mathrm{eff}} = U - J$ is the only meaningful parameter. The self-consistent linear response calculation introduced by Cococcioni et al.[44] was adopted to determine *U*. In this way, a Hubbard correction of $U = 3.28$ eV is found (see Supplementary Methods), which is close to the $U_{Bulk} = 3$ eV value found in bulk V_2O_3 system[45], which is then applied throughout the paper.

The magnetic and electronic self-consistent calculations were performed with a total energy convergence criterion of 10^{-6} eV with the BZ sampled by a denser 24 × 24 × 1Γ-centered *k*-point mesh. The spin–orbit coupling (SOC) was included by a second variational procedure on a fully self-consistent basis. To test the sensitivity of the results to the choice of the functional, the local density approximation (LDA)[46] and the screened exchange hybrid density functional by Heyd–Scuseria–Ernzerhof (HSE06)[47] are employed. In addition, for the substrate calculations, the van der Waals (vdW) interactions were taken into account by the use of Grimme's DFT-D3 method[48]. The phonon dispersion was calculated self-consistently on the basis of the density-functional perturbation theory (DFPT) and with the use of the PHONOPY package[49].

Monte-Carlo simulations

The ab initio molecular dynamic (AIMD) simulations were carried out on a 4 × 4 × 1 supercell at 300 K in the canonical ensemble using the Nose–Hoover thermostat approach[50,51] with 3000 times steps of step size 2 fs. The Curie temperature was estimated by Monte-Carlo (MC) simulations, as implemented in the VAMPIRE package[52]. For these calculations, a rectangular $100 \times 100\sqrt{3}$ supercell was used, where the spins were thermalized for 10^4 equilibrium steps, followed by 2×10^4 averaging steps to calculate the thermal-averaged magnetization for each temperature. The atomic structures were visualized by the VESTA program[53].

DATA AVAILABILITY

The data that support the findings of this study are provided here and in the Supplementary Information.

CODE AVAILABILITY

The codes that are necessary to reproduce the findings of this study are available from the corresponding author upon reasonable request. All DFT calculations were performed by using the Vienna ab initio simulation package (VASP).

Received: 6 January 2021; Accepted: 15 June 2021;
Published online: 09 July 2021

REFERENCES

1. Wang, J., Deng, S., Liu, Z. & Liu, Z. The rare two-dimensional materials with Dirac cones. *Natl. Sci. Rev.* **2**, 22–39 (2015).
2. Wallace, P. R. The band theory of graphite. *Phys. Rev.* **71**, 622–634 (1947).
3. Bolotin, K. et al. Ultrahigh electron mobility in suspended graphene. *Solid State Commun.* **146**, 351 – 355 (2008).
4. Zhang, Y., Tan, Y.-W., Stormer, H. L. & Kim, P. Experimental observation of the quantum hall effect and berry's phase in graphene. *Nature* **438**, 201–204 (2005).
5. Du, X., Skachko, I., Duerr, F., Luican, A. & Andrei, E. Y. Fractional quantum hall effect and insulating phase of Dirac electrons in graphene. *Nature* **462**, 192–195 (2009).
6. Novoselov, K. S. et al. Electric field effect in atomically thin carbon films. *Science* **306**, 666–669 (2004).
7. Chu, Y.-H. Van der waals oxide heteroepitaxy. *npj Quant. Mater.* **2**, 67 (2017).
8. Choudhury, T. H., Zhang, X., Al Balushi, Z. Y., Chubarov, M. & Redwing, J. M. Epitaxial growth of two-dimensional layered transition metal dichalcogenides. *Annu. Rev. Mater. Res.* **50**, 155–177 (2020).
9. Haldane, F. D. M. Model for a quantum hall effect without Landau levels: condensed-matter realization of the "parity anomaly". *Phys. Rev. Lett.* **61**, 2015–2018 (1988).
10. Kane, C. L. & Mele, E. J. Quantum spin hall effect in graphene. *Phys. Rev. Lett.* **95**, 226801 (2005).
11. Wang, H. P., Luo, W. & Xiang, H. J. Prediction of high-temperature quantum anomalous hall effect in two-dimensional transition-metal oxides. *Phys. Rev. B* **95**, 125430 (2017).
12. Guo, Y., Clark, S. J. & Robertson, J. Calculation of metallic and insulating phases of V_2O_3 by hybrid density functionals. *J. Chem. Phys.* **140**, 054702 (2014).
13. Song, T. T. et al. The stability of aluminium oxide monolayer and its interface with two-dimensional materials. *Sci. Rep.* **6**, 29221 (2016).
14. Song, T. T. et al. Graphene stabilized high-k dielectric Y_2O_3(111) monolayers and their interfacial properties. *RSC Adv.* **5**, 83588–83593 (2015).
15. van Gog, H. et al. Thermal stability and electronic and magnetic properties of atomically thin 2d transition metal oxides. *npj 2D Mater. Appl.* **3**, 18 (2019).
16. Surnev, S. et al. Growth and structure of ultrathin vanadium oxide layers on Pb (111). *Phys. Rev. B* **61**, 13945–13954 (2000).
17. Whangbo, M.-H., Gordon, E. E., Xiang, H., Koo, H.-J. & Lee, C. Prediction of spin orientations in terms of homo-lumo interactions using spin–orbit coupling as perturbation. *Acc. Chem. Res.* **48**, 3080–3087 (2015).
18. Tiwari, S., Van de Put, M. L., Sorée, B. & Vandenberghe, W. G. Critical behavior of the ferromagnets CrI_3, $CrBr_3$, and $CrGeTe_3$ and the antiferromagnet $FeCl_2$: a detailed first-principles study. *Phys. Rev. B* **103**, 014432 (2021).
19. Wang, X. L. Proposal for a new class of materials: Spin gapless semiconductors. *Phys. Rev. Lett.* **100**, 156404 (2008).
20. Liu, C.-C. et al. Low-energy effective hamiltonian for giant-gap quantum spin hall insulators in honeycomb X-hydride/halide (X = N − Bi) monolayers. *Phys. Rev. B* **90**, 085431 (2014).
21. Molle, A. et al. Buckled two-dimensional xene sheets. *Nat. Mater.* **16**, 163–169 (2017).
22. Mellaerts, S. et al. Quarter-filled Kane-mele Hubbard model: Dirac half metals. *Phys. Rev. B* **103**, 155159 (2021).
23. Mellaerts, S. Topological Effects in 2D Strongly Correlated Electron Systems. KU Leuven. Faculteit Wetenschappen (2020).
24. Guo, Y., Clark, S. J. & Robertson, J. Calculation of metallic and insulating phases of V_2O_3 by hybrid density functionals. *J. Chem. Phys.* **140**, 054702 (2014).
25. Guo, Y., Clark, S. J. & Robertson, J. Electronic and magnetic properties of Ti_2O_3, Cr_2O_3, and Fe_2O_3 calculated by the screened exchange hybrid density functional. *J. Phys. Condens. Matter* **24**, 325504 (2012).
26. Griffith, J. & Orgel, L. Ligand-field theory. *Q. Rev. Chem. Soc.* **11**, 381–393 (1957).
27. Yu, M. & Trinkle, D. R. Accurate and efficient algorithm for Bader charge integration. *J. Chem. Phys.* **134**, 064111 (2011).
28. Fukui, T., Hatsugai, Y. & Suzuki, H. Chern numbers in discretized Brillouin zone: efficient method of computing (spin) hall conductances. *J. Phys. Soc. Japan.* **74**, 1674–1677 (2005).
29. Zhang, G.-F., Li, Y. & Wu, C. Honeycomb lattice with multiorbital structure: topological and quantum anomalous hall insulators with large gaps. *Phys. Rev. B* **90**, 075114 (2014).
30. Castro Neto, A. H., Guinea, F., Peres, N. M. R., Novoselov, K. S. & Geim, A. K. The electronic properties of graphene. *Rev. Mod. Phys.* **81**, 109–162 (2009).
31. Díaz-Fernández, A., Chico, L., González, J. W. & Domínguez-Adame, F. Tuning the fermi velocity in dirac materials with an electric field. *Sci. Rep.* **7**, 8058 (2017).
32. Homm, P., Menghini, M., Seo, J. W., Peters, S. & Locquet, J. P. Room temperature mott metal-insulator transition in V_2O_3 compounds induced via strain-engineering. *APL Mater.* **9**, 021116 (2021).
33. Goniakowski, J. & Noguera, C. Properties of metal-supported oxide honeycomb monolayers: M_2O_3 and MM'_2O_3 on Me(111) (M, M = Ti, V, Cr, Fe; Me = Ag, Au, Pt). *J. Phys. Chem. C* **124**, 8186–8197 (2020).
34. Liu, Z., Wang, J. & Li, J. Dirac cones in two-dimensional systems: from hexagonal to square lattices. *Phys. Chem. Chem. Phys.* **15**, 18855–18862 (2013).
35. Addou, R., Dahal, A. & Batzill, M. Growth of a two-dimensional dielectric monolayer on quasi-freestanding graphene. *Nat. Nanotechnol.* **8**, 41–45 (2013).
36. Li, P. & Cai, T.-Y. Two-dimensional transition-metal oxides Mn_2O_3 realized the quantum anomalous hall effect. *J. Phys. Chem. C* **124**, 12705–12712 (2020).
37. Hashmi, A., Nakanishi, K., Farooq, M. U. & Ono, T. Ising ferromagnetism and robust half-metallicity in two-dimensional honeycomb-kagome Cr_2O_3 layer. *npj 2D Mater. Appl.* **4**, 39 (2020).
38. Wang, S., Goniakowski, J., Noguera, C. & Castell, M. R. Atomic and electronic structure of an epitaxial Nb_2O_3 honeycomb monolayer on Au (111). *Phys. Rev. B* **100**, 125408 (2019).
39. Wang, S., Hu, X., Goniakowski, J., Noguera, C. & Castell, M. R. Influence of the support on stabilizing local defects in strained monolayer oxide films. *Nanoscale* **11**, 2412–2422 (2019).
40. Kresse, G. & Furthmüller, J. Efficient iterative schemes for ab initio total-energy calculations using a plane-wave basis set. *Phys. Rev. B* **54**, 11169–11186 (1996).
41. Perdew, J. P., Burke, K. & Ernzerhof, M. Generalized gradient approximation made simple. *Phys. Rev. Lett.* **77**, 3865–3868 (1996).
42. Kresse, G. & Joubert, D. From ultrasoft pseudopotentials to the projector augmented-wave method. *Phys. Rev. B* **59**, 1758–1775 (1999).
43. Dudarev, S. L., Botton, G. A., Savrasov, S. Y., Humphreys, C. J. & Sutton, A. P. Electron-energy-loss spectra and the structural stability of nickel oxide: An LSDA +U study. *Phys. Rev. B* **57**, 1505–1509 (1998).
44. Cococcioni, M. & de Gironcoli, S. Linear response approach to the calculation of the effective interaction parameters in the LDA + U method. *Phys. Rev. B* **71**, 035105 (2005).
45. Grieger, D. & Fabrizio, M. Low-temperature magnetic ordering and structural distortions in vanadium sesquioxide V_2O_3. *Phys. Rev. B* **92**, 075121 (2015).
46. Ceperley, D. M. & Alder, B. J. Ground state of the electron gas by a stochastic method. *Phys. Rev. Lett.* **45**, 566–569 (1980).
47. Krukau, A. V., Vydrov, O. A., Izmaylov, A. F. & Scuseria, G. E. Influence of the exchange screening parameter on the performance of screened hybrid functionals. *J. Chem. Phys.* **125**, 224106 (2006).
48. Grimme, S., Antony, J., Ehrlich, S. & Krieg, H. A consistent and accurate ab initio parametrization of density functional dispersion correction (dft-d) for the 94 elements h-pu. *J. Chem. Phys.* **132**, 154104 (2010).
49. Togo, A. & Tanaka, I. First principles phonon calculations in materials science. *Scr. Mater.* **108**, 1–5 (2015).
50. Hoover, W. G. Canonical dynamics: equilibrium phase-space distributions. *Phys. Rev. A* **31**, 1695–1697 (1985).
51. Nose, S. A unified formulation of the constant temperature molecular dynamics methods. *J. Chem. Phys.* **81**, 511–519 (1984).
52. Evans, R. F. L. et al. Atomistic spin model simulations of magnetic nanomaterials. *J. Phys. Condens. Matter* **26**, 103202 (2014).
53. Momma, K. & Izumi, F. *VESTA3* for three-dimensional visualization of crystal, volumetric and morphology data. *J. Appl. Crystallogr.* **44**, 1272–1276 (2011).

ACKNOWLEDGEMENTS

Part of this work was financially supported by the KU Leuven Research Funds, Project No. KAC24/18/056 and No. C14/17/080 as well as the Research Funds of the INTERREG-E-TEST Project (EMR113) and INTERREG-VL-NL-ETPATHFINDER Project (0559). Part of the computational resources and services used in this work were provided by the VSC (Flemish Supercomputer Center) funded by the Research Foundation Flanders (FWO) and the Flemish government.

AUTHOR CONTRIBUTIONS

These results were obtained within the framework of a master thesis supervised by J.-P.L. and M.H. S.M. performed all DFT calculations mentored by R.M. The manuscript was written by S.M. with contributions and comments from all authors.

COMPETING INTERESTS

The authors declare no competing interests.

ADDITIONAL INFORMATION

Supplementary information The online version contains supplementary material available at https://doi.org/10.1038/s41699-021-00245-w.

Correspondence and requests for materials should be addressed to S.M.

Reprints and permission information is available at http://www.nature.com/reprints

Publisher's note Springer Nature remains neutral with regard to jurisdictional claims in published maps and institutional affiliations.